nature electronics

Article

https://doi.org/10.1038/s41928-022-00859-y

An organic artificial spiking neuron for in situ neuromorphic sensing and biointerfacing

In the format provided by the authors and unedited

Table of contents page

Molecular doping with DEMTA for optimization of the PEDOT:PSS dispersion

The aqueous dispersion of PEDOT:PSS (Hereaus, Clevios PH 1000) was modified by adding 15 wt% N-methyl-2,2'-diaminodiethylamine (DEMTA, TCI), 5 wt% ethylene glycol (EG, Sigma Aldrich) and 1 wt% (3-glycidyloxypropyl) trimethoxysilane (GOPS, Sigma Aldrich)[1]. Mixing the dispersion after each addition for 20 s and if necessary, cooling with an ice bath is required to avoid de-doping reaction of PEDOT during the modification process. The dispersion was filtered through a PVDF-filter (pore size 0.45 µm) and further spin coated at 1500 RPM for 2 min. The devices were annealed at 120 °C for 20 min.

Ion-selective OANs

2.5 wt.% Potassium ionophore III (Sigma Aldrich), 0.5 wt.% potassium tetrakis(4-chlor-ophenyl-)borate (Sigma Aldrich) and 60.5 wt% diisodecyl adipate (Sigma Aldrich) was added to 36.5 wt% poly(vinylchloride) (PVC, high M_W, Fluka) and dissolved in tetrahydrofuran (THF, 500 mg/5 mL). The solution was drop-casted on a glass slide, while the membrane dimension is defined by a rubber ring. To implement the resulting ion-selective membrane(s) into the device a PDMS well was used to confine the filling solution (100 mM NaCl). As analyte, KCl and NaCl solution were measured at various concentrations 100, 200, 500 mM, starting from low concentration. The ion-selective membrane(s) is incorporated in the T_1 OECT forming ion-specific OANs.

Dopamine-induced neuronal excitation

Dulbecco's phosphate buffered saline (PBS, Sigma Alrich), consisting of NaCl (137.89 mM), KH_2PO_4 (1.47 mM), NaH_2PO_4 (8.10 mM) and KCl (2.68 mM) in DI-water, was used as the electrolyte. Dopamine hydrochloride (Sigma Alrich) was dissolved in DI-water to obtain a 3.5 mM stock solution. Then in the PBS solution the respective volume of dopamine solution was introduced to obtain various concentrations 0.1, 0.25, 0.5, 1.0 mM, starting from dopamine solution with low concentration. Dopamine-based

neuronal excitation/inhibition was induced by exposing the solution to the T_1 of the OAN. Between each measurement step the OAN was cleaned with deionized water for 3 min.

Cell culture and biohybrid neurons

Commercial Transwell-filters (area=1.12 cm^2, pore size=0.4 µm) were modified by collagen coating to enhance cell attachment before seeding Caco-2 cells (DSMZ, ACC 169) with $1.5 \cdot 10^5$ cells/insert. Cells were cultured in culture medium EMEM (Eagle's Minimum Essential Medium, Invitrogen) with 10 vol.% FBS (fetal bovine serum, Invitrogen), 1 vol.% glutamine (GlutaMax-1, 100X, Invitrogen) and 1 vol.% Pen-strep (10000 $\mu g \cdot mL^{-1}$ penicillin, 10000 $\mu g \cdot mL^{-1}$ streptomycin, Invitrogen) as additives. Cells were maintained at 37 °C in a humidified atmosphere with 5 % CO2 during cell culturing and with a medium change every 2 to 3 days[2-4]. A representative optical microphotograph of the cell culture process is shown in Fig. 4A. Caco-2 cells (i.e., the bio-membrane), seeded in a Transwell-filter, were integrated into the T_1 device(s) with Phosphate buffer saline (PBS, Sigma Aldrich) as the filling solution and analyte to the barrier tissue. Experiments were performed on day 14 after seeding, having a Trans-Epithelial Resistance (TER) of 400 $\Omega \cdot cm^2$, measured with a Volt-Ohm meter EVOM2 (World Precision Instruments). The bio-membrane was incorporated via the Transwell-filter in the T_1 device, forming the biohybrid neuron. The bio-membrane of the biohybrid neuron was disrupted by adding the toxin H_2O_2 (746.47 mM, Sigma Aldrich) to the analyte.

Supplementary Figures

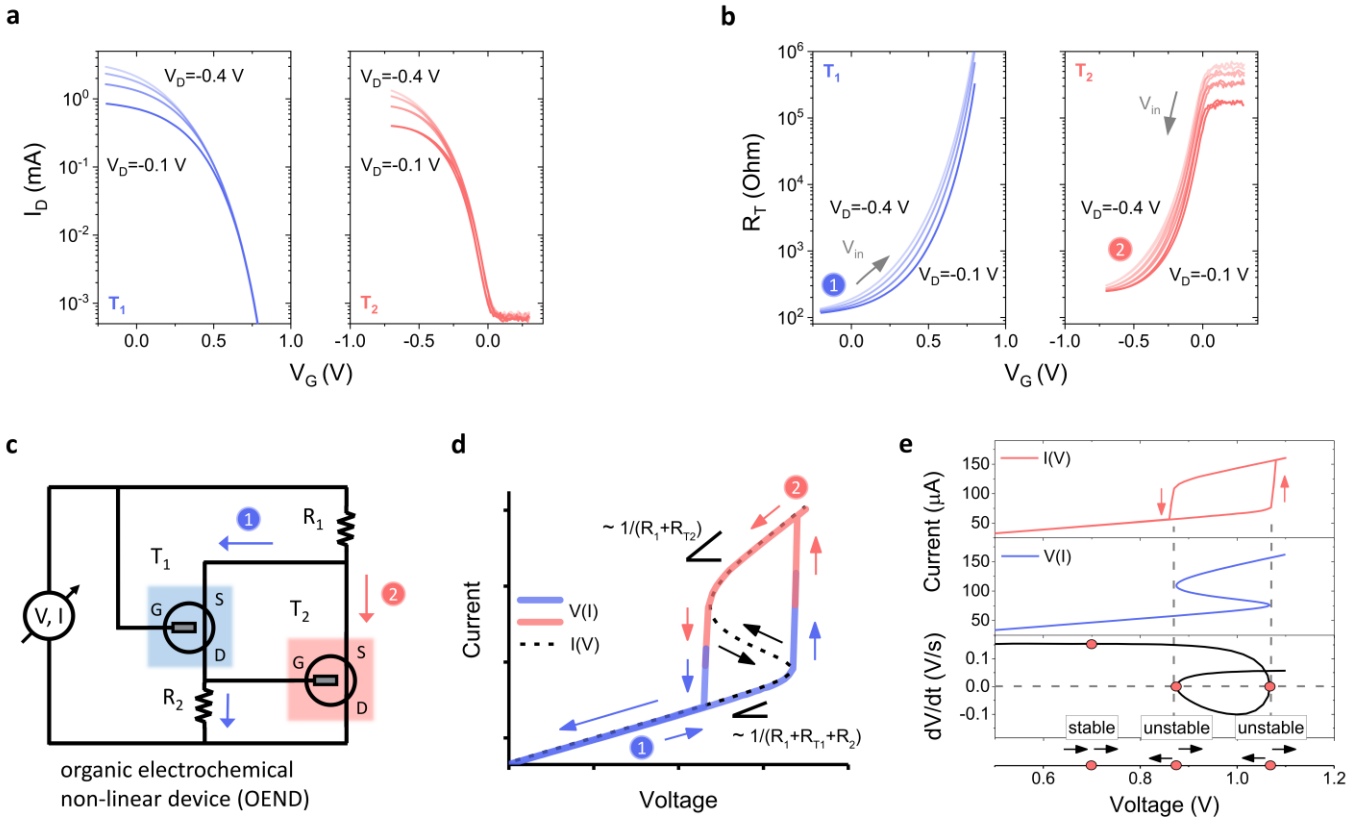

Supplementary Fig. 1 l Device characteristics and the response of the organic electrochemical OEND. a, Transfer characteristics of the T_1 (p-type OECT, depletion mode, PEDOT:PSS-based) and T_2 (p-type OECT, enhancement mode, p(g2T-TT)-based) transistors for $V_D = -0.1, -0.2, -0.3, -0.4\,V$. **b**, Channel resistance R_T vs gate voltage V_G of T_1 and T_2. **c**, Circuit diagram of the OEND. The cascade-like configuration of T_1 and T_2, their output current in in competition (see also b; for increasing V_{in}, R_{T1} is increasing and R_{T2} is decreasing). The ratio of the channel resistances R_{T2}/R_{T1} defines the dominant current path (here indicated as ①, ②). **d**, Schematic of the Current-Voltage characteristics of the OEND in the $V(I)$ and $I(V)$ mode. In the $V(I)$ mode, the S-shaped NDR region is stable, as the $V(I)$ is a single-valued function. In the $I(V)$ mode, the S-shaped NDR region is unstable, as the $I(V)$ is a multi-valued function and a sharp current switch is observed at the boarders of the S-shaped NDR region. The lower and upper linear (ohmic-like) regions define the current range of the Current-Voltage characteristic. ①: Lower linear region (resistance $\cong 1/(R_1 + R_{T1} + R_2)$). ②: Upper linear region (resistance $\cong$

$1/(R_1 + R_{T2})$). **e**, Stability analysis. Operational stability is shown at the $^{dV}/_{dt}$ vs $Voltage$ plot. Outside the S-shaped NDR region, operation points are stable, as small-amplitude $Voltage$ perturbations lead to the shift of $Voltage$ towards the same direction (see also black errors on the bottom). At the borders of the S-shaped NDR region, operation points are unstable, as small-amplitude $Voltage$ perturbations lead to the shift of $Voltage$ towards opposite directions. This operational instability leads to the abrupt switch of current (at the unstable points) of the $V(I)$ mode.

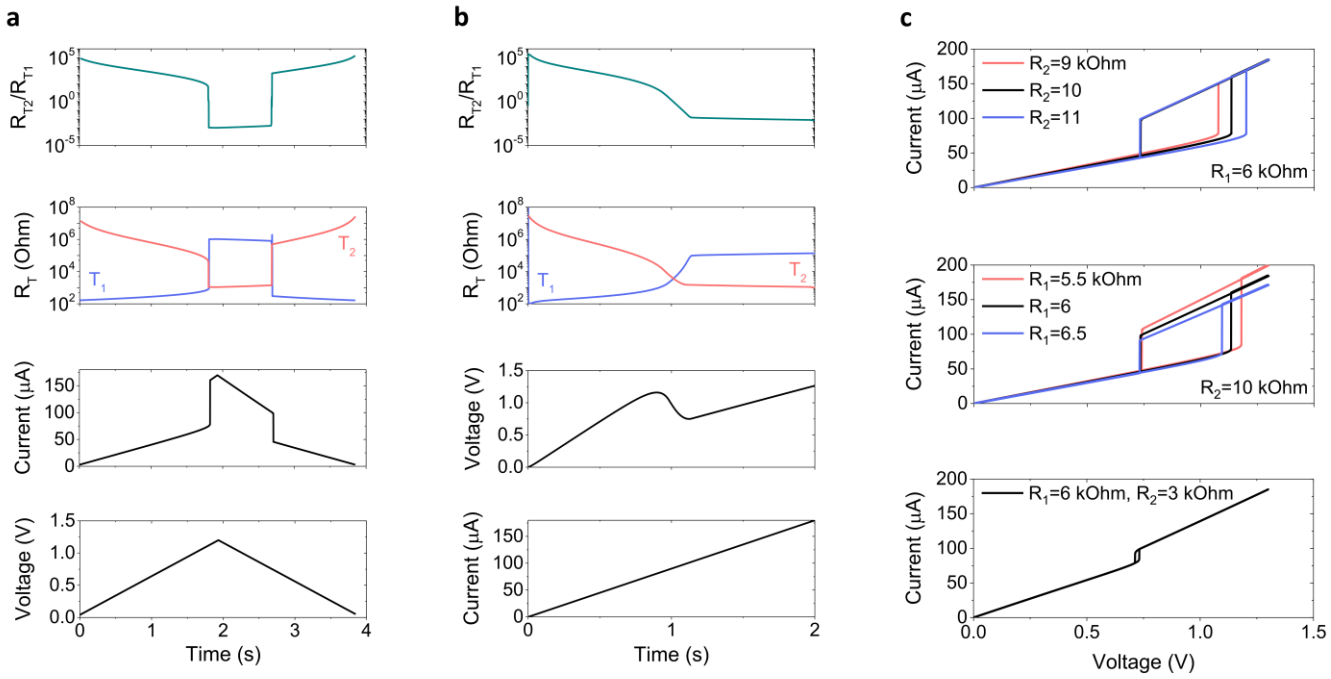

Supplementary Fig. 2 | Simulations of the temporal response of the OEND. a, $V(I)$ and **b**, $I(V)$ mode. Briefly, due to the cascade-like configuration of T_1 and T_2 in the OEND, the output of the first transistor (source-drain voltage of T_1, V_{DS1}) feeds the input of the next one (source-gate voltage of T_2, V_{GS2}), and their responses are thus in competition. This competition defines the dominant pathway of current flowing through T_1 or T_2, as the independent input variable (I or V) is enforced. In the $I(V)$ mode, switching in the pathway from T_1 to T_2 occurs when the transistors obtain comparable values of channel resistance ($R_{T1} \cong R_{T2}$). The switching is accompanied by a sharp vertical transition in the $I(V)$ plane from the high ($R_1 - R_{T1} - R_2$) to the low resistance pathway ($R_1 - R_{T2}$) and vice-versa. In the $V(I)$ mode, the non-linearity in the transition from T_1 to T_2 pathway and vice-versa (i.e., non-linear temporal change of the ratio R_{T2}/R_{T1}), gives rise to the non-monotonic temporal response of the voltage V, and therefore to the emergence of the S-shaped NDR regime in the $V(I)$ plane. Circuit simulations of the OEND are performed for threshold voltage $V_{th,T1} = 600\,mV$ and $V_{th,T2} = 0\,mV$ for the transistors T_1 and T_2 respectively, $R_1 = 6\,kOhm$ and $R_2 = 10\,kOhm$. **c**, Effect of the resistor value R_1 and R_2 at the $V(I)$ characteristic. As shown in the Supplementary Fig. 1c, switching in the $V(I)$ characteristic means a change in the dominant current path ①, ②. In more detail, the upper and lower linear nodes of the $V(I)$s are

directly related to the values of R_1 and R_2. The slope of the upper linear node depends on R_1 (lower R_1 leads to a steeper upper slope), while the slope of the lower linear node depends on $R_1 + R_2$ (lower $R_1 + R_2$ leads to a stepper lower slope). On parallel, the switching voltage from the current path ① to ② also shifts when changing the value of $R_1 + R_2$. For instance, when R_2 is increasing (for fixed $R_1 = 6\ kOhm$), the switching voltage is increasing, as higher input voltage in required in order to balance the equivalent resistance between current path ① and ② via the T_1 and T_2. When R_1 is increasing (for fixed $R_2 = 10\ kOhm$), the switching voltage is decreasing, as lower input voltage in required in order to balance the equivalent resistance between current path ① and ②. In the extreme (non-functional) case of $R_2 < R_1$, the upper and lower linear regions collapse into an almost non-hysteretic behavior.

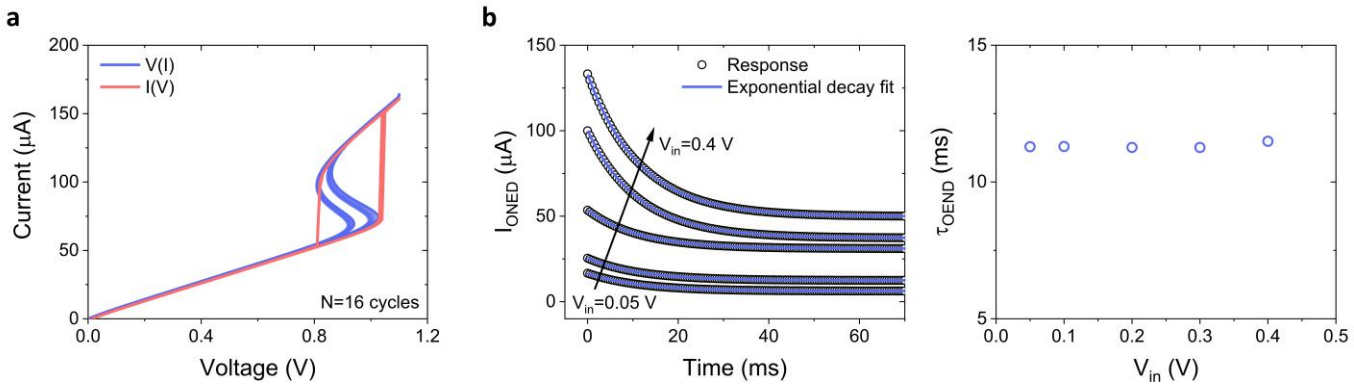

Supplementary Fig. 3 | Response of the OEND. a, Stability of non-linear phenomena. Consecutive scans in the $V(I)$ or $I(V)$ mode of the OEND for $N = 16$ cycles. **b**, Time response τ_{OEND} of the OEND element under square input pulses of different amplitude ($V_{in} = 0.05 - 0.4\,V$, at $t = 0$). The time response τ_{OEND} is extracted by fitting the transient current I_{OEND} vs $Time$ with an exponential decay function ($I_{OEND} = I_0 + Ae^{-\frac{t}{\tau_{OEND}}}$).

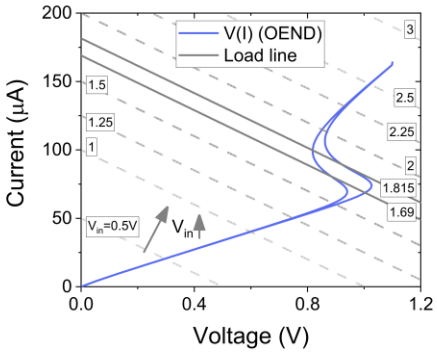

Supplementary Fig. 4 l Load line analysis. S-shaped NDR characteristic and load line analysis for load resistor $R = 10\ kOhm$ and $V_{in} = 0.5 - 3\ V$. The resistance of R is selected to be equal or greater that the differential resistance Δr of the OEND ($-8\ kOhm \leq \Delta r \leq 15\ kOhm$). Under this condition, electrochemical oscillations occur when the load line is within the S-shaped NDR region, e.g., for this representative example $V_{in} = 1.69 - 1.815\ V$.

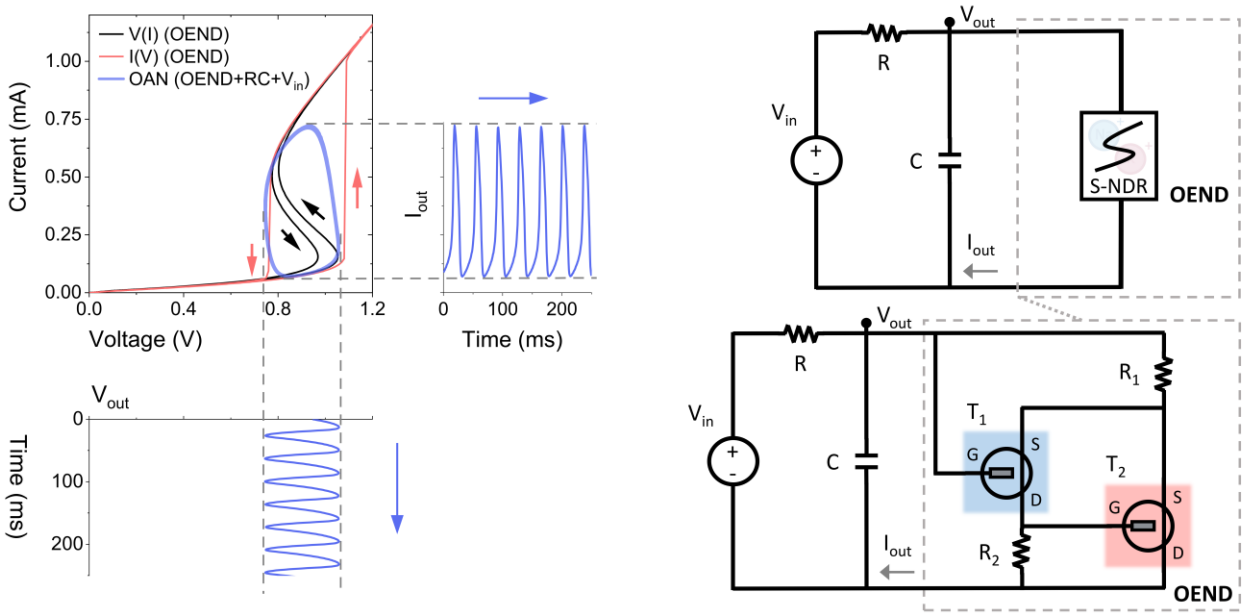

Supplementary Fig. 5 | Non-linear phenomena and electrochemical oscillations. $Current$ vs $Voltage$ characteristic in the in the $V(I)$ or $I(V)$ mode of the OEND, along with the parametric plot of the electrochemical oscillations. V_{out} and I_{out} is the resulting voltage and current respectively of the OEND device, under the influence of the input voltage V_{in}. The parametric plot is expanded into the time domain components, i.e., V_{out} vs $Time$ and I_{out} vs $Time$. Voltage and current oscillations propagate over time and their amplitude lies withing the S-shaped NDR region. The circuit diagram of the OAN is shown, along with the analogy to the OEND device.

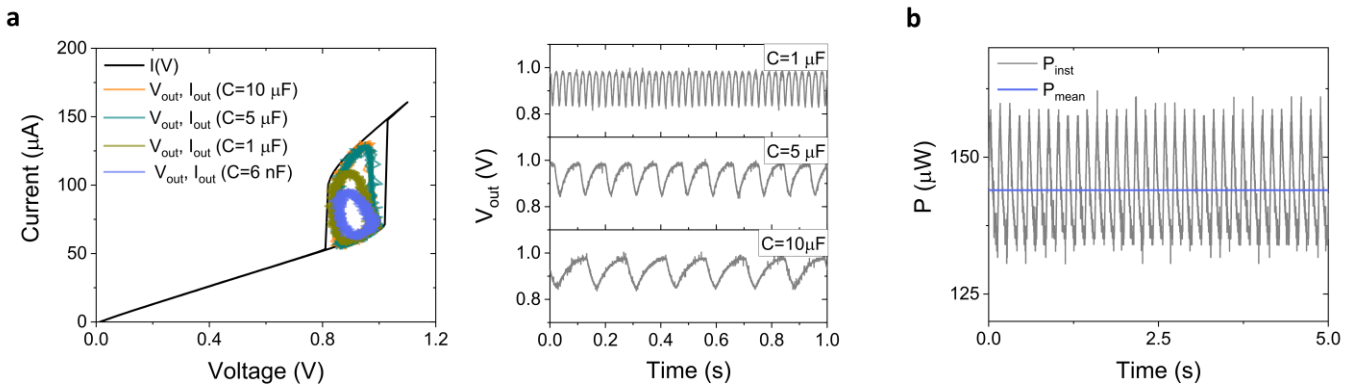

Supplementary Fig. 6 l Characteristics of the electrochemical oscillations. **a**, $Current$ vs $Voltage$ characteristic of the OEND, along with the parametric oscillatory response (V_{out}, I_{out}) for different capacitors, $C = 6\ nF - 10\ \mu F$. The temporal V_{out} response, V_{out} vs $Time$ is also shown. **b**, Instantaneous $P_{inst} = {V_{in}}/{R}\ (V_{in} - V_{out})$ and mean P_{mean} ($\cong 143\ \mu W$) power dissipation or the organic spiking neuron for $C = 10\ \mu F$. P_{mean} is is calculated as $P_{mean} = f_{fir} \times \int_0^T P_{inst}(t)dt$.

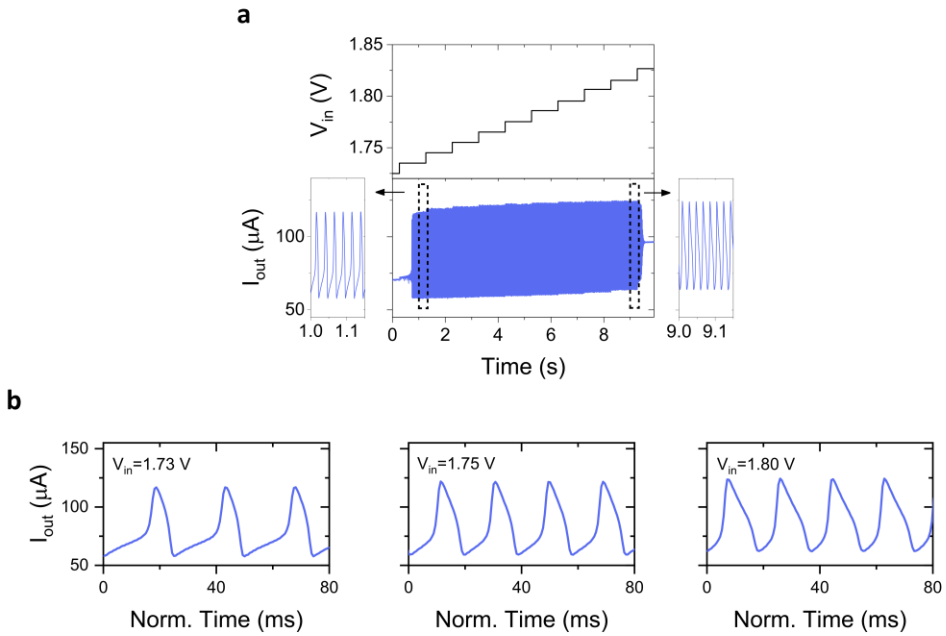

Supplementary Fig. 7 l Voltage-controlled oscillator. a, Temporal firing response I_{out} under the V_{in} bias. The OANs behaves like a voltage-controlled oscillator (VOC). V_{in} is changed from 1.72 V to 1.82 V with a step equal to ~10 mV and I_{out} changes accordingly. **b**, detailed spiking waveform as a function of V_{in} ($V_{in} = 1.73,\ 1.75,\ 1.80\ V$). For each graph, the time axis is normalised to a common waveform phase $\varphi = 0$. All measurements are obtained with a capacitance $C = 1\ \mu F$.

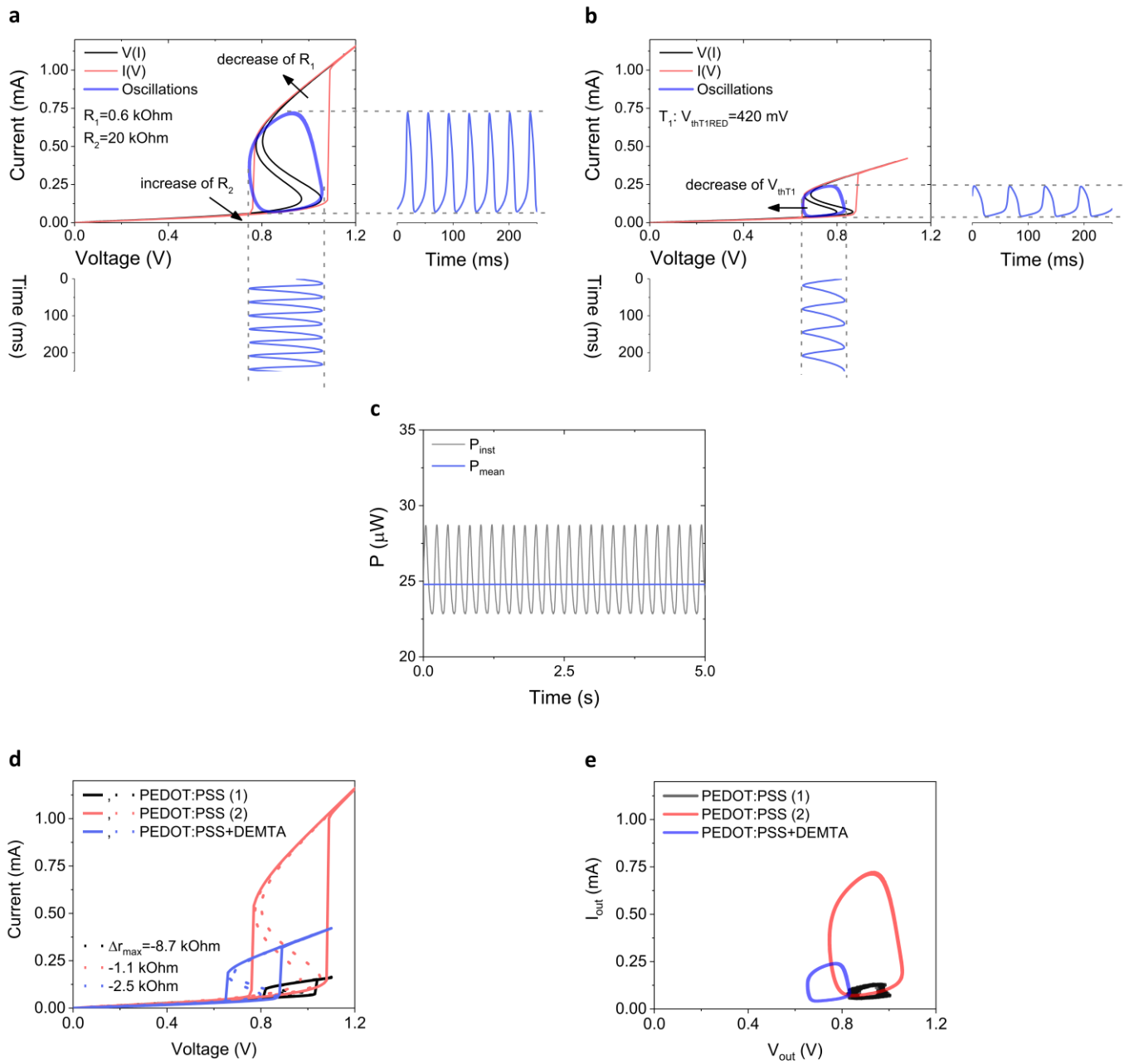

Supplementary Fig. 8 | Engineering the OEND and oscillation characteristics. a, The oscillatory current window at the y axis can be adjusted by changing the resistors R_1 and R_2 (here $R_1 = 20\ kOhm$ and $R_2 = 0.6\ kOhm$). **b**, The amplitude and the offset of the voltage oscillations at the x axis can be engineered by decreasing the threshold of the transistor T1, $V_{thT1RED} = 420\ mV$ (initially from $V_{thT1} = 600\ mV$). The V_{thT1} is decreased by doping PEDOT:PSS with the amine-based molecular dopant DEMTA. **c**, Instantaneous P_{inst} and mean P_{mean} ($\cong 24\ \mu W$) power dissipation or the organic spiking neuron for $C =$

$10\ \mu F$, in the case of the reduced $V_{thT1RED}$ of b. **d**, $I(V)$ and $V(I)$ characteristics obtained by engineering the NDR slope, Δr. **e**, Resulting parametric oscillatory response.

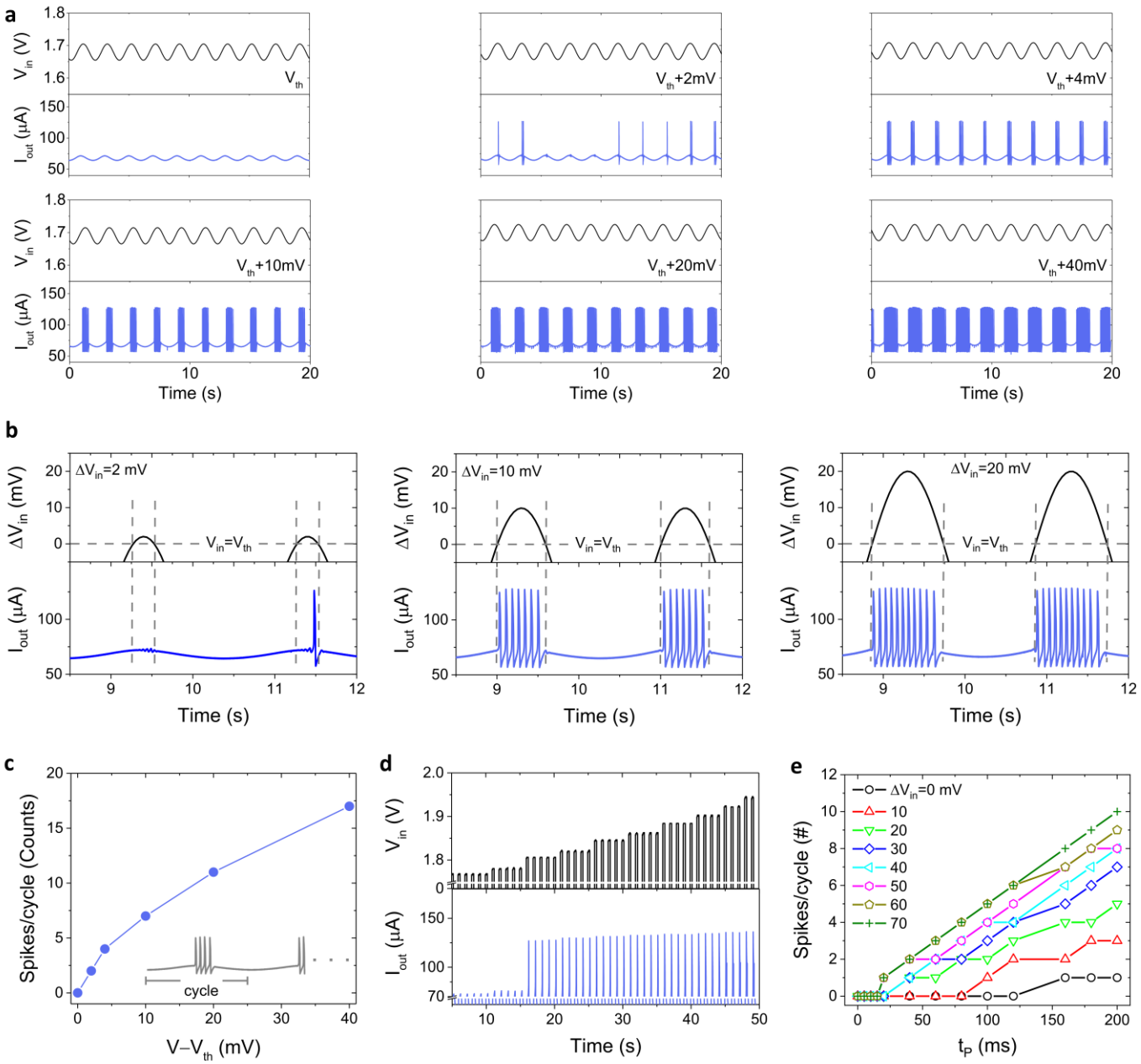

Supplementary Fig. 9 l Neuro-inspired functions. a, Electrochemical oscillation-mediated neuronal firing for different DC voltages above the firing threshold V_{th}. V_{th} is the threshold of the OAN, the maximum input voltage where no oscillation behavior is displayed. Neuronal firing is phase-locked with the electrochemical oscillations at the electrolyte medium. **b**, Detailed phase-dependent spiking response of the AON. The neuron receives a sinusoidal input signal V_{in} that is 2, 10 and 20 mV higher than the threshold V_{th} of OAN firing. The firing of the OAN is coordinated within this time window and therefore the OAN exhibits phase-dependent firing. **c**, $Spikes/cycle$ vs $V - V_{th}$ for electrochemical oscillations with

various DC offset $V - V_{th}$. **d**, *In-liquid* all-or-nothing spiking, e.g., spikes are elicited only when V_{in} reaches a certain threshold V_{th}. **e**, $Spikes/cycle$ vs t_P (pulse width) for different square pulses of amplitude ΔV_{in} (=$V - V_{th}$). For a given amplitude ΔV_{in} the $Spikes/cycle$ increase with the pulse width t_P. As ΔV_{in} is increasing, shorter pulses (lower t_P) initiate spiking.

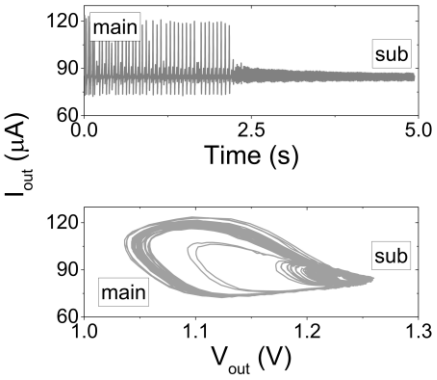

Supplementary Fig. 10 l Subthreshold oscillations. Main spiking and subthreshold oscillations of the OAN. Upper: time domain response of output current I_{out}. Lower: Parametric plot, V_{out} vs I_{out}.

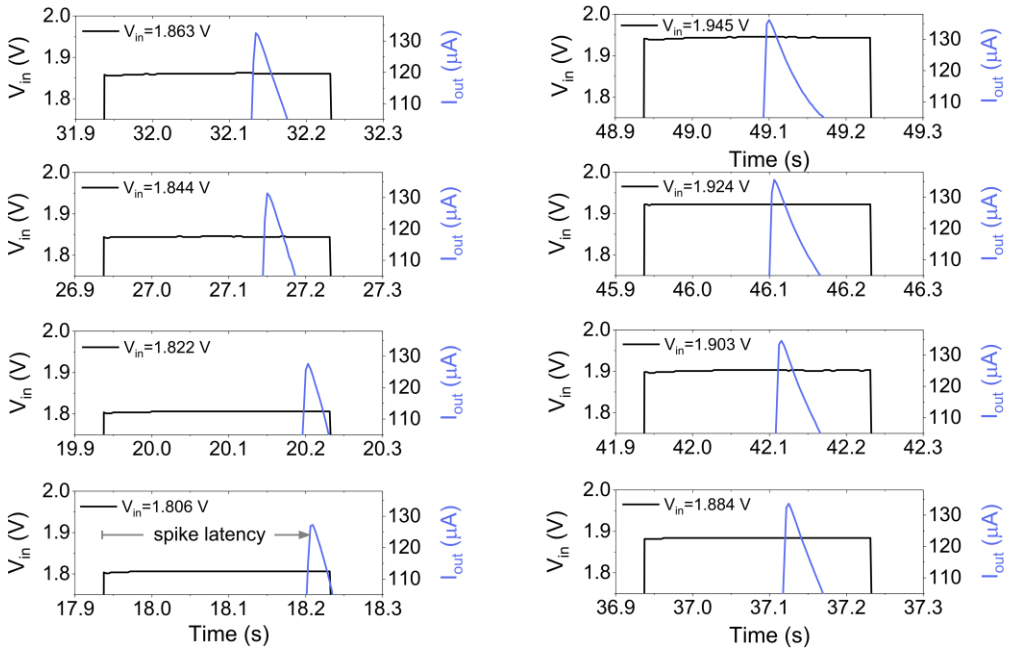

Supplementary Fig. 11 | *In-liquid* spike latency. Time difference (or spike latency) between the onset of an input voltage pulse V_{in} ($V_{in} = 1.806 - 1.945\ V, time\ width = 260\ ms$) and the occurrence of a spike. The spike latency is defined as the time difference between the beginning of the input voltage pulse and the peak of the OAN output current spike. The spike latency can also be expressed as a phase difference $\Delta\varphi$ the beginning of the input voltage pulse and the peak of the OAN output current spike, $\Delta\varphi = 2\pi\left({spike\ latency}/{T}\right)$, where T the time width of the input voltage pulse.

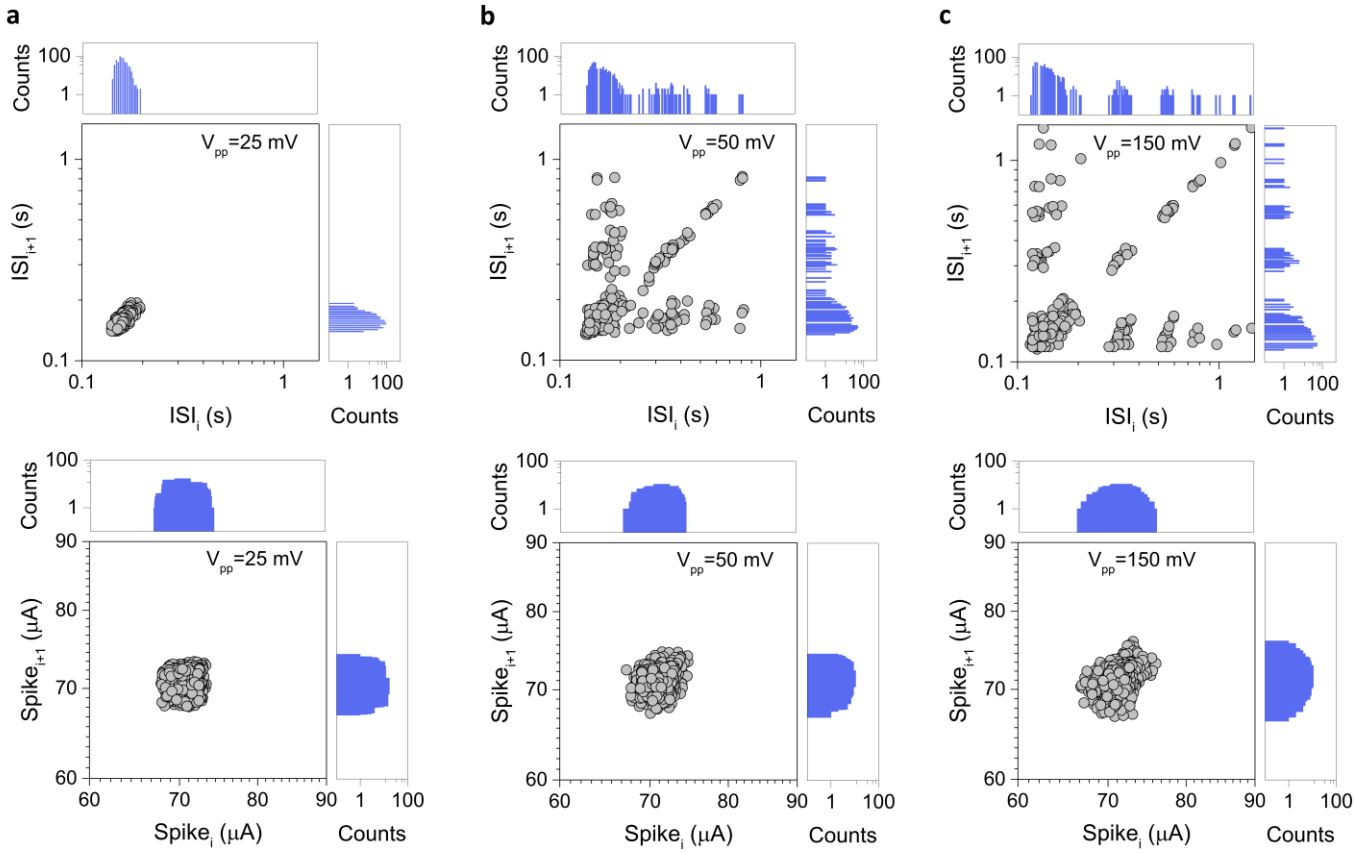

Supplementary Fig. 12 | Recurrence plots and noise at the electrolyte medium. Recurrence plots of the interspike intervals (ISI_i vs ISI_{i+1}) and spike-to-spike amplitudes ($Spike_i$ vs $Spike_{i+1}$) for injecting white noise at the electrolyte of amplitude V_{pp}. **a**, $V_{pp} = 25\,mV$. **b**, $V_{pp} = 50\,mV$. **c**, $V_{pp} = 150\,mV$. The interspike histograms are unimodal for low-noise and gradually spread and separate as the noise level increases, thus forming clusters. These clusters of interspike intervals followed by quiescence periods, indicate a change in coding from tonic firing to noise-induced bursting. Despite the noisy conditions, the spike-to-spike amplitude plots ($Spike_i$ vs $Spike_{i+1}$) show low spreading as a function of the noise level, highlighting the robustness of spiking against noise at the electrolytic medium.

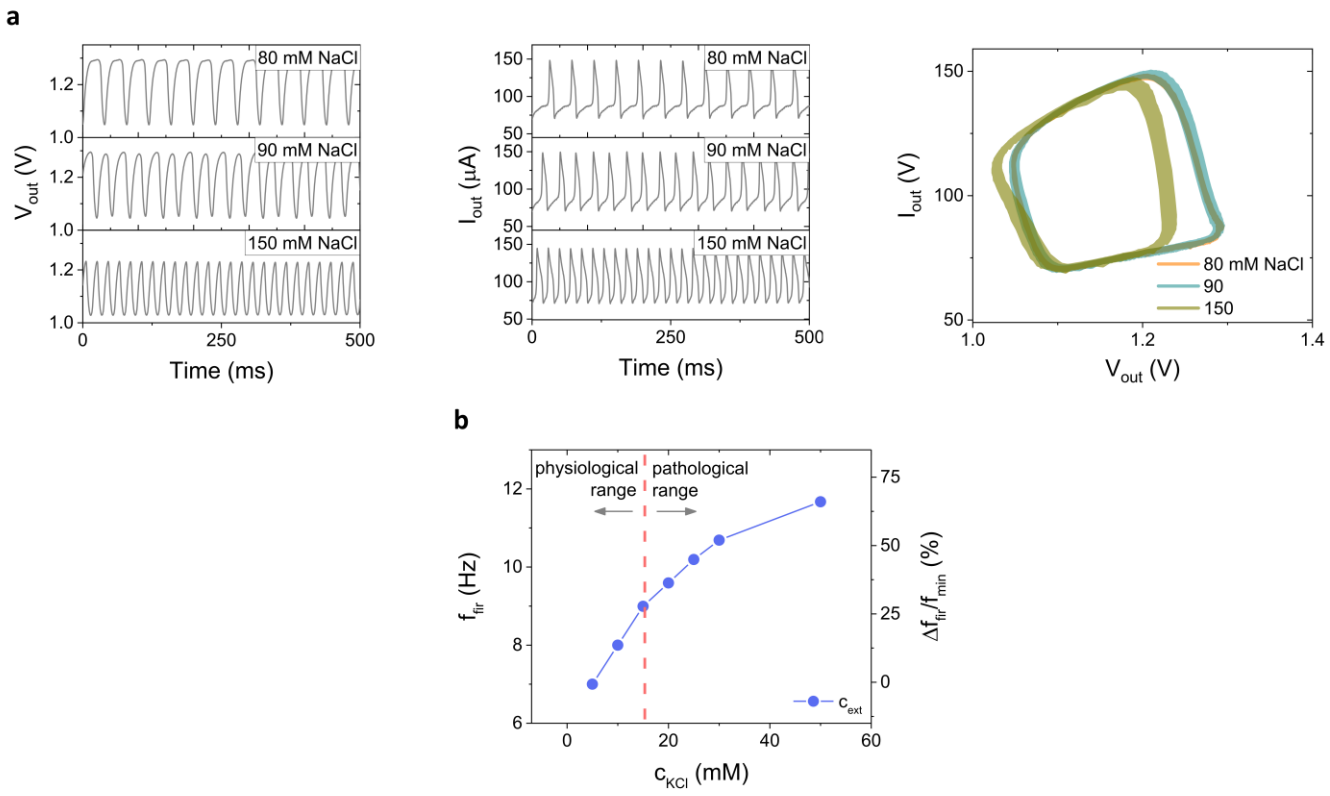

Supplementary Fig. 13 l Electrolyte concentration-dependent firing response. a, V_{out} vs $Time$, I_{out} vs $Time$ and parametric oscillatory plot (Lissajous-like) of the OAN for different ionic concentrations (aqueous NaCl), $c = 80, 90, 150\, mM$ NaCl. **b**, Firing frequency f_{fir} of the OAN as a function of KCl concentration. The range of extracellular K^+ concentrations under common physiological and pathological conditions in the brain is also indicated.

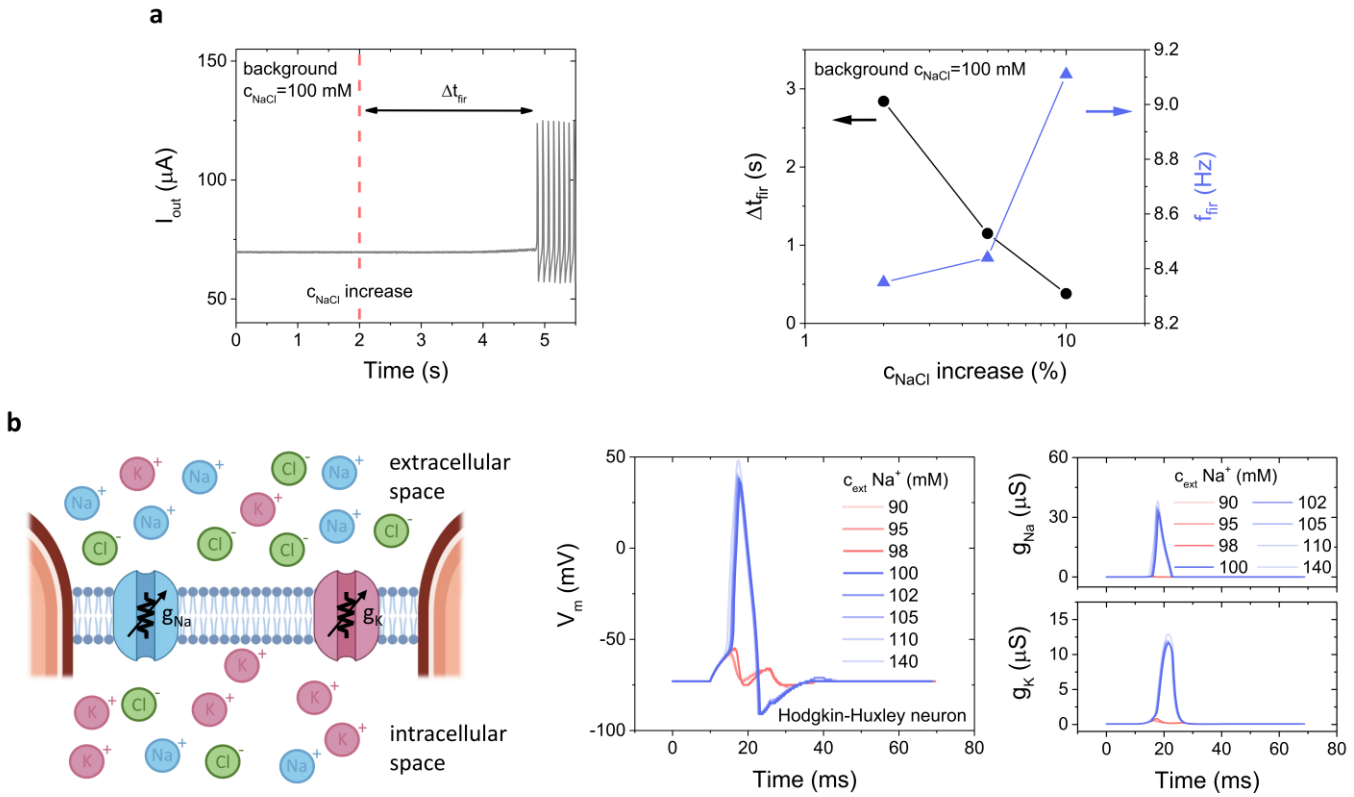

Supplementary Fig. 14 l Electrolyte concentration-neuronal excitability and firing properties. a, (Left) Electrolyte-induced excitability of the AON. Minute perturbations of NaCl ionic concentrations c_{NaCl}, ranging from 2% to 10%, over the physiologically-relevant baseline ($100\ mM\ NaCl$) enhances neuronal excitability and initiate tonic spiking with a stimulus-firing time delay Δt_{fir}. (Right) Stimulus-firing time delay Δt_{fir} and firing frequency f_{fir} as a function of the NaCl concentration, c_{NaCl}. **b**, Simulations of the action potential waveform as a function of the extracellular Na^+ concentration based on the Hodgkin-Huxley neuronal model. Simulations of the temporal evolution of the conductance g_{Na}, g_K of the Na^+ and K^+ channels is also shown. Action potentials are initiated as the extracellular Na^+ concentration is increased with threshold at $c_{Na} \cong 100\ mM$. Simulation parameters: Na^+: $c_{int} = 15\ mM$, $c_{ext} = 90 - 140\ mM$. K^+: $c_{int} = 150\ mM$, $c_{ext} = 4\ mM$. Cl^-: $c_{int} = 5\ mM$, $c_{ext} = 120\ mM$. c_{int} is the intracellular ion concentration and c_{ext} is the extracellular ion concentration. Stimulus: current clamp mode for $I_s = 5\ nA$. Simulation parameters are selected to be in physiologically relevant levels.

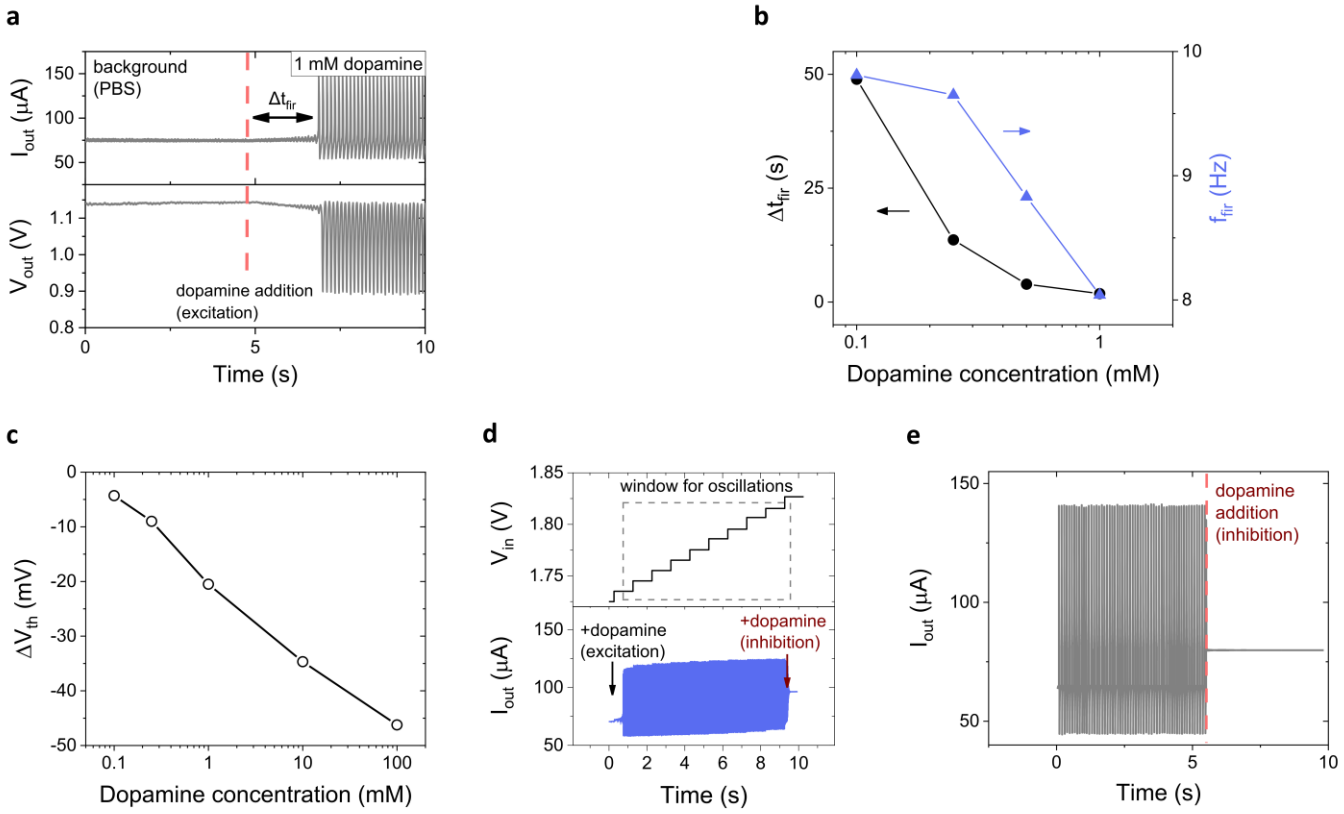

Supplementary Fig. 15 l Neurotransmitter-induced neuronal excitation/inhibition. a, Dopamine-induced excitability of the OAN. Minute perturbations of dopamine $(0.1 - 1\,mM)$ in PBS solution enhances neuronal excitability and initiate tonic spiking with a stimulus-firing time delay Δt_{fir}. **b**, Stimulus-firing time delay Δt_{fir} and firing frequency f_{fir} as a function of dopamine concentration. **c**, Sensing dopamine with the PEDOT:PSS T_1 transistor. the addition of dopamine (positively charged DA^+ in the aqueous solution) shifts the threshold voltage V_{th} of the transistor to lower voltages (with ΔV_{th}, the threshold voltage difference). **d**, Window for oscillations of the OAN. Outside of this window oscillations cease. The OAN biasing conditions define the type of neuronal behaviour (excitatory/inhibitory). When the OAN is biased the below the window for oscillations, the OAN is susceptible to dopamine-induced excitation. When the OAN is biased at the upper regime of the window for oscillations, the OAN is susceptible to dopamine-induced inhibition. *Excitation:* the OAN is biased that the lower limit of the window. At this biasing condition, the addition of dopamine lowers V_{th} and oscillations are triggered (the window for oscillations shifts effectively towards lower input voltages). *Inhibition:* the OAN is biased at the upper limit

of the window and the AON already oscillates. The addition of dopamine lowers the V_{th}, the window for oscillations still shifts effectively towards lower input voltages and in this case this leads to the OAN inhibition. **e**, Dopamine-induced inhibition of the OAN (the addition of dopamine stops the OAN oscillations).

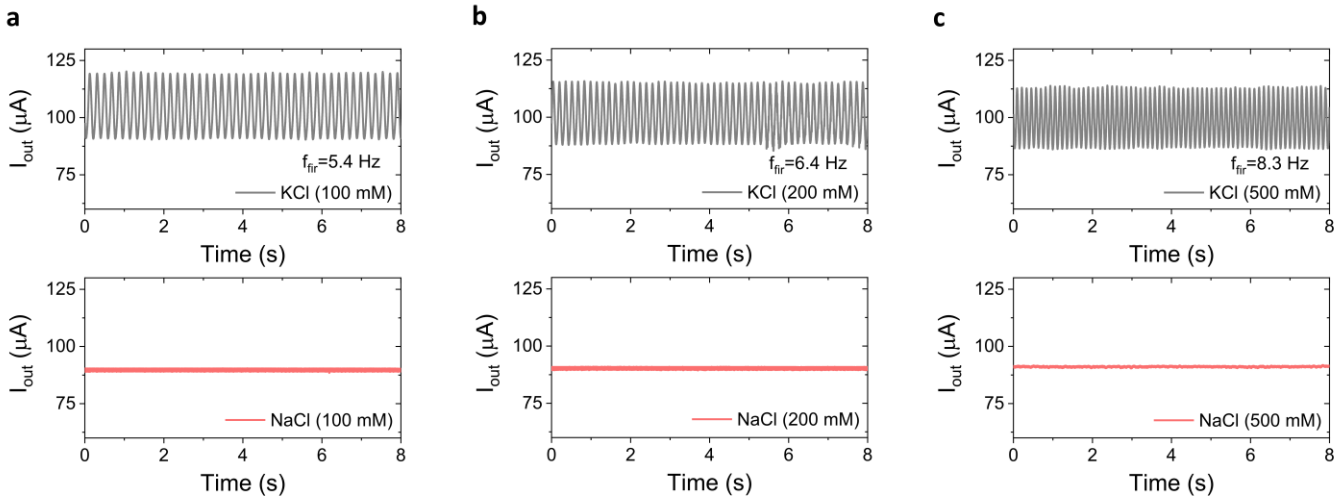

Supplementary Fig. 16 l Ion-selective oscillations for emulating *in-liquid* ion channel dynamics. K^+ ion-selective OAN induce ion specific oscillations. OAN is insensitive to Na^+ ions. **a**, $c = 100\ mM$ KCl and $c = 100\ mM$ NaCl. **b**, $c = 200\ mM$ KCl and $c = 200\ mM$ NaCl. (C) $c = 500\ mM$ KCl and $c = 500\ mM$ NaCl. The KCl selectivity is retained even for high NaCl concentrations. In the case of the KCl electrolyte, the firing frequency f_{fir} can be still modulated via the ion-selective membrane by increasing the KCl concentration.

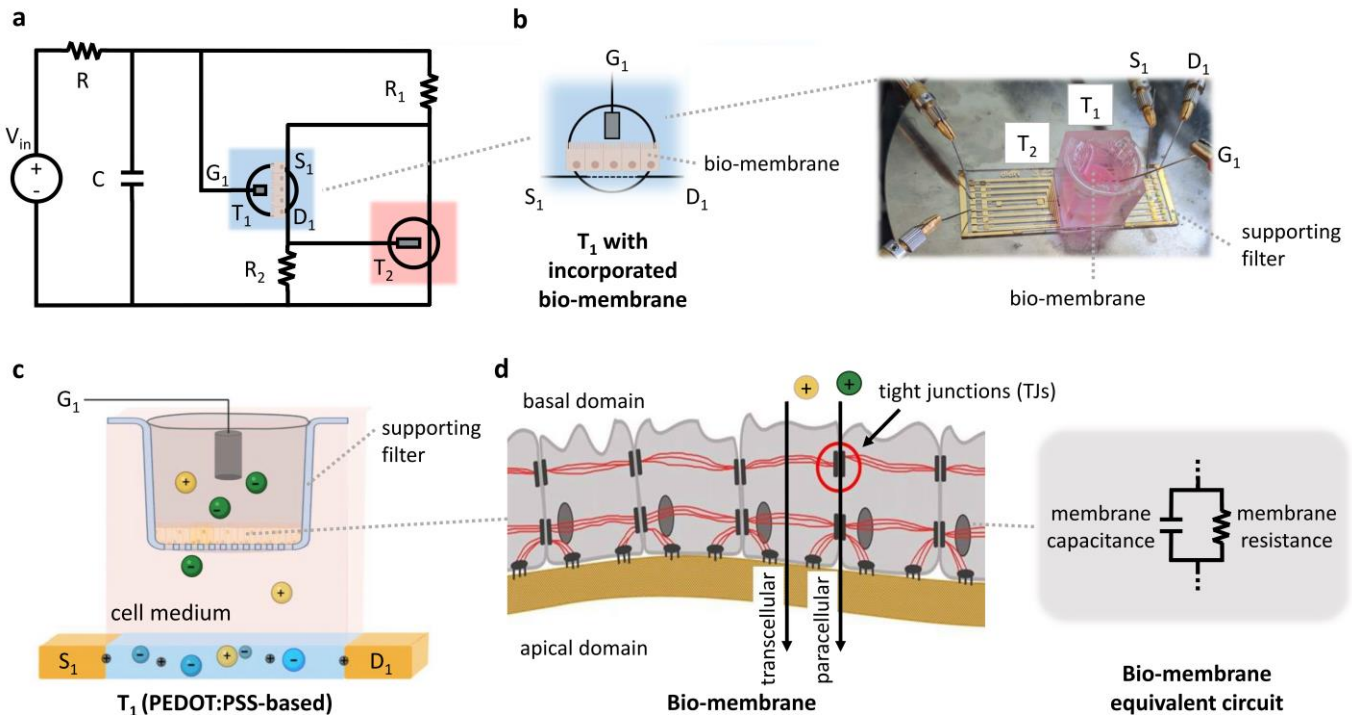

Supplementary Fig. 17 l Detailed schematic of the biohybrid neuron. a, Circuit diagram of the biohybrid neurons consisting of an OAN with incorporated bio-membrane. **b**, Schematic and optical photograph of the T_1 with the bio-membrane. The bio-membrane is incorporated between the gate (G_1) and channel of the T_1 transistor. **c**, Side view schematic of the T_1 with the bio-membrane showing the different components of the system (T_1, transwell filter, bio-membrane, cell medium). **d**, Schematic of epithelial cell layer (bio-membrane) that functions as a physical barrier for ion passage between the basal and apical domain. Cells are attached together by intercellular tight junctions (TJs) forming a barrier for ion passage through the membrane. Ion passage has to potential pathways, the transcellular (through cells) and the paracellular (between cells) pathway. Toxins such as peroxide (H_2O_2) attack the TJs, thus affecting the paracellular pathway for ion passage. The equivalent circuit of the bio-membrane is a parallel RC circuit, with R the transmembrane resistance and C the membrane capacitance. Toxins such as peroxide (H_2O_2) attack the TJs, facilitate the transmembrane ion passage, and decrease R and C. In an OECT configuration, TJ disruption (i.e., the decrease of the *RC*) effectively means a decrease of the OECT threshold voltage. In a biohybrid neuron that is initially biased below the threshold for firing, the addition of H_2O_2 will disrupt

the bio-membrane's TJs and will initiate the OAN firing (due to the lowering of the threshold voltage of T_1 with the disrupted bio-membrane).

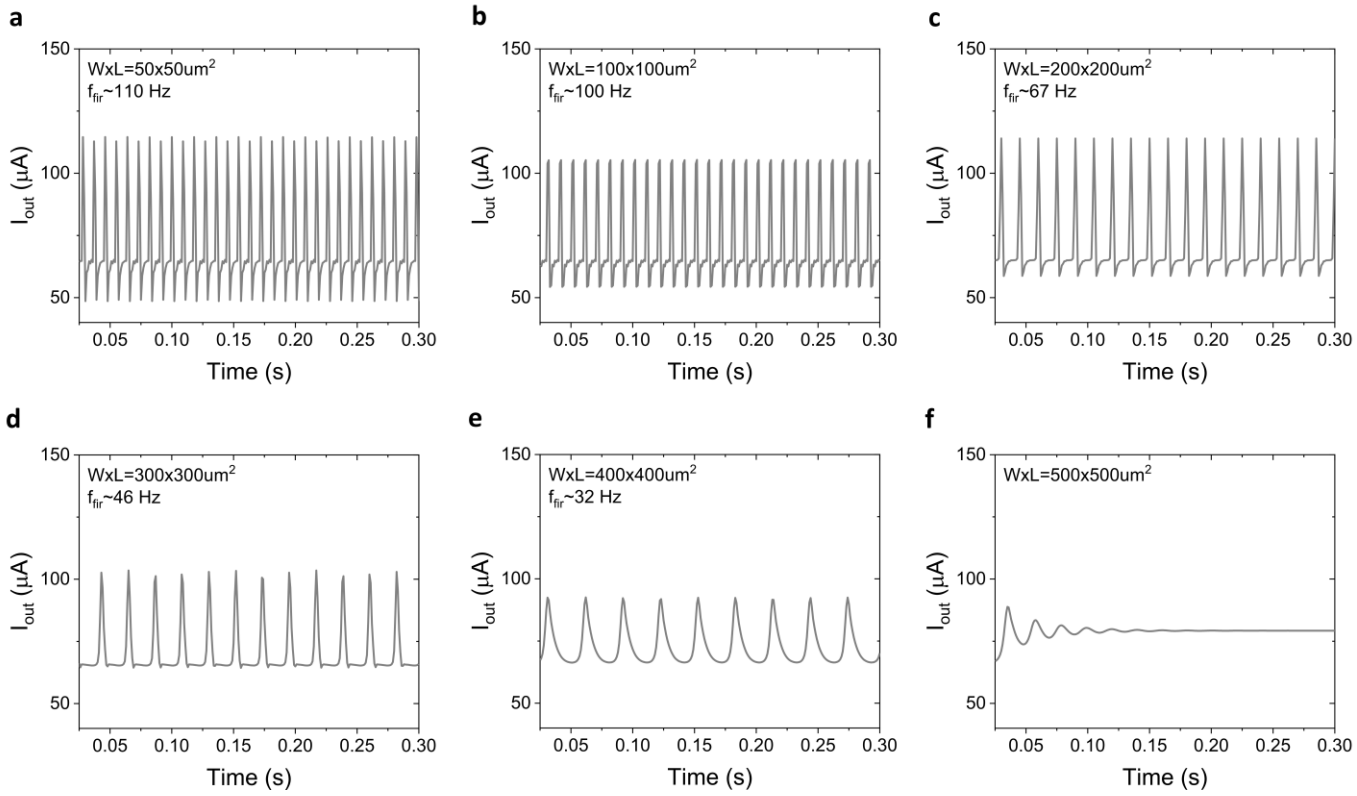

Supplementary Fig. 18 l OAN Spiking properties and device dimensions. Simulations of the spiking response of the AON, I_{out} vs $Time$ for different device dimension *W* and *L*. *W* and *L* are de channel width and length respectively. The simulations were performed for channel thickness $t = 100\ nm$ (polymer film thickness) and $C = 120\ nF$ (load capacitance of the OAN). **a**, $WxL = 50x50\ \mu m^2$. **b**, $WxL = 100x100\ \mu m^2$. **c**, $WxL = 200x200\ \mu m^2$. **d**, $WxL = 300x300\ \mu m^2$. **e**, $WxL = 400x400\ \mu m^2$. **f**, $WxL = 500x500\ \mu m^2$. As the device dimensions increase (and therefor the channel capacitance), the spiking frequency of the OAN is decreasing. In the limiting case of very large channels the energy dissipation dominates the OAN fails to bifurcate showing only decaying dynamics.

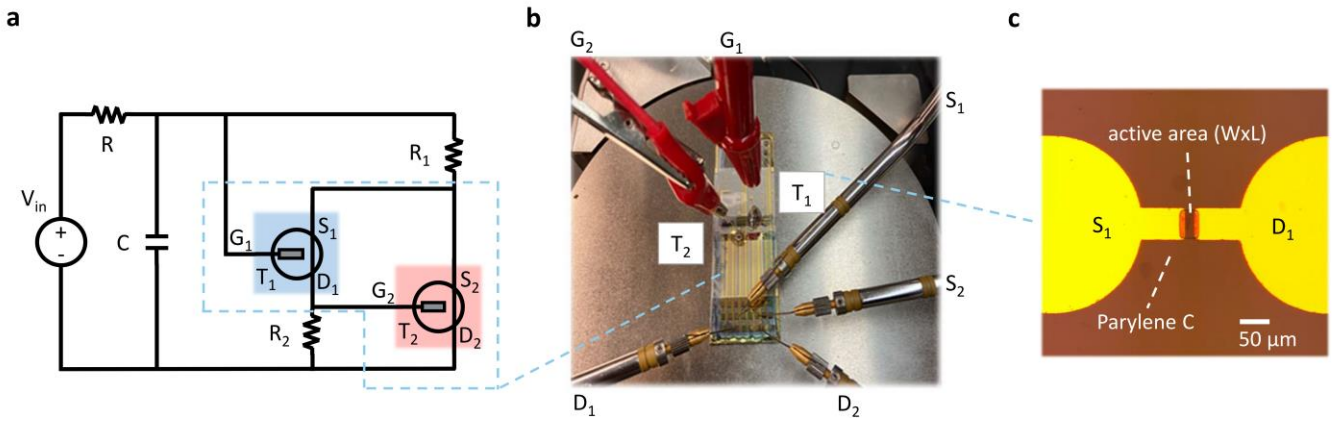

Supplementary Fig. 19 l Circuit diagram and optical photographs of the OAN. a, Circuit diagram of the OAN. For the implementation of the AON. **b**, Optical photograph of the microfabricated T_1 and T_2 transistors on a common glass substrate (described in the methods section). For the formation of the OAN, the components R_1, R_2, C, V_{in} are connected externally. **c**, Photomicrograph of the T_1 transistor channel with active area dimensions of $W \times L = 50 \times 20\,\mu m^2$. The active area is exposed to the wetware (i.e., electrolyte), while the rest of the structure is insulated with a layer of Parylene C. (S) source, (D) drain, (G) gate terminals.

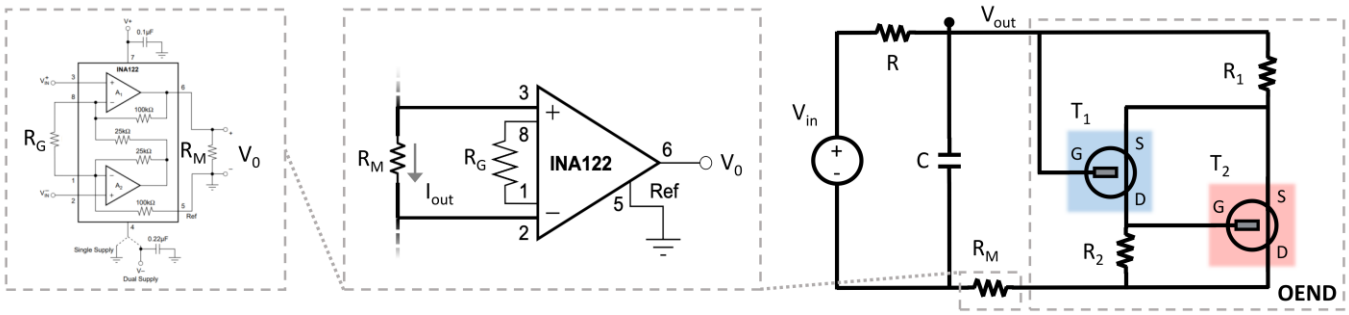

Supplementary Fig. 20 l Measuring the output current of the OAN. The output current I_{out} of the OEND is measured by measuring the voltage V_0 across a resistor R_M with a differential amplifier (based on an INA122 IC, Texas Instruments) and a digital oscilloscope. By selecting $R_G = 10\,kOhm$ and $R_M = 100\,Ohm$, the voltage gain of the amplifier is $G = 25$. The output current I_{out} of the OEND is $I_{out} = {V_0}/{(G \cdot R_M)}$. The resistor value of R_M was kept much lower than the rest of the circuit components in order to avoid the effect of R_M on the circuit operation.

Neuron type	Materials	Phenomena	Topology	Wetware operation	*In situ* ion sensing	*In situ* bio-interfacing	Components (#)	Spiking frequency (Hz)	Power consumption (µW)		Min feat. size (µm)	Biophysical realism
									dyn. max.	mean		
Mulaosmanovic et al.[5]	Ferroelectric	Polarization	Transistor-like, switching	No	No	No	1T	NA	NR	NR	0.03	No
Inagaki et al.[6]	Multi-component	Photonic	Multi-component	No	No	No	Multi-component	$1.\cdot10^{3}$-$8.0\cdot10^{3}$	NR	NR	NA	Partially
Torrejon et al.[7]	Ferromagnetic	Spintronic	Diode-like	No	No	No	1D	$250\cdot10^{6}$-$400\cdot10^{6}$	NR	1	0.375	No
Abu-Hassan et al.[8]	Silicon	Electronic	Multi-component IC	No	No	No	Multi-T	~1-270	$85\cdot10^{-3}$	$75\cdot10^{-3}$	0.18	Yes
Hao et al.[9]	2D	Filament-based	Diode-like, switching	No	No	No	1D	NA	NR	NR	0.5	No
Bohaichuk et al.[10]	Hybrid	Mott MIT	Diode-like, NDR	No	No	No	1D, 1R, 1C	$0.7\cdot10^{6}$-$2.7\cdot10^{6}$	NR	NR	0.3	Partially
Yi et al.[11]	Metal-oxide	Mott MIT	Diode-like, NDR	No	No	No	2D, 2R, 2C-3C, 2 V_{int}	~$5\cdot10^{3}$-$50\cdot10^{3}$	NR	2	0.05	Yes
Zhang et al.[12]	Metal-oxide	Mott MIT	Diode-like, NDR	No	No	No	1D, 1R, 1C	$0.4\cdot10^{6}$-$0.9\cdot10^{6}$	39	28	~20	Partially
Park et al.[13]	Metal-oxide	Vacancy-based	Diode-like	No	No	No	1D	NA	35	NR	5	Partially
Pickett et al.[14]	Metal-oxide	Mott MIT	Diode-like, NDR	No	No	No	2D, 3R, 3C	~$8\cdot10^{3}$-$28\cdot10^{3}$	NR	NR	0.11	Partially
Kumar et al. (2017)[15]	Metal-oxide	Mott MIT	Diode-like, NDR	No	No	No	1D, 1R, 1C	~$30\cdot10^{3}$-$70\cdot10^{3}$	NR	NR	~0.1	Yes
Kumar et al. (2020)[16]	Metal-oxide	Mott MIT	Diode-like, NDR	No	No	No	1D	~$2\cdot10^{6}$-$9\cdot10^{6}$	NR	NR	~0.1	Yes
Tee et al.[17]	Organic	Electronic	Inverter-like, RO	No	No	No	8T-12T, 1R	50-200	4.5	NR	NR	Partially
Hosseini et al.[18]	Organic	Electronic	Inverter-like, RO	No	No	No	9T, 2C, 1R	0.4-5	40	NR	30	Partially
Harikesh et al.[19]	Organic	Ionoelectronic	Inverter-like	Yes	Yes	No	5T, 2C	0.06-0.25	15	NR	200	Partially
This work	Organic	Ionoelectronic	Transistor-like, NDR	Yes	Yes	Yes	2T, 2R, 1C	5-55	28	24	10	Yes

Supplementary Table 1. l State-of-the-art of various technologies of artificial (spiking) neurons. Abbreviations: Mott metal-insulator transition (Mott MIT), negative differential resistance (NDR), ring oscillator (RO), diode (D), resistor (R), capacitor (C), transistor (T), internal voltage source (V_{int}), not (directly) reported (NR), not applicable (NA).

Neuron type	Threshold	VCO/ CCO	Ion excitation/inhibition	Ion selectivity	Neurotransmitter excitation/inhibition	Noise-induced spiking	Firing mode				Subthreshold oscillations	Spike latency	Spike integration
							tonic	phasic	bursting	mixed mode			
Inagaki et al.[6]	Yes	Yes	No	No	No	No	Yes	Yes	No	No	Yes	No	No
Abu-Hassan et al.[8]	Yes	Yes	No	No	No	No	Yes	Yes	Yes	No	No	No	No
Bohaichuk et al.[10]	Yes	Yes	No	No	No	No	Yes	No	No	No	No	No	No
Yi et al.[11]	Yes	Yes	No	No	No	Yes	Yes	Yes	Yes	Yes	Yes	Yes	Yes
Zhang et al.[12]	Yes	Yes	No	No	No	No	Yes	Yes	No	No	No	No	No
Park et al.[13]	Yes	No	No	No	No	No	No	No	No	No	No	Yes	Yes
Pickett et al.[14]	Yes	Yes	No	No	No	No	Yes	No	No	No	No	No	No
Kumar et al. (2017)[15]	Yes	Yes	No	No	No	Yes	Yes	Yes	Yes	Yes	Yes	No	No
Kumar et al. (2020)[16]	Yes	Yes	No	No	No	Yes	Yes	Yes	Yes	Yes	Yes	No	No
Tee et al.[17]	Yes	Yes	No	No	No	No	Yes	No	No	No	No	No	No
Hosseini et al.[18]	Yes	Yes	No	No	No	No	Yes	No	No	No	No	No	No
Harikesh et al.[19]	Yes	Yes	No	No	No	No	Yes	No	No	No	No	No	No
This work	Yes	Yes	Yes (Na^+, K^+ excitation/inhibition)	Yes (Na^+, K^+)	Yes (dopamine excitation/inhibition)	Yes	Yes	Yes	Yes	No	Yes	Yes	Yes

Supplementary Table 2. l Reported characteristics of artificial neurons with biophysical realism. Entries from the Supplementary Table 1 are shown here that are at least partially biophysically realistic. Abbreviations: Voltage-controlled oscillator (VCO), current-controlled oscillator (CCO).

References

1 Keene, S. T. *et al.* Enhancement-Mode PEDOT:PSS Organic Electrochemical Transistors Using Molecular De-Doping. *Adv. Mater.* **32**, 2000270 (2020).

2 Sambuy, Y. *et al.* The Caco-2 cell line as a model of the intestinal barrier: influence of cell and culture-related factors on Caco-2 cell functional characteristics. *Cell Biol. Toxicol.* **21**, 1-26 (2005).

3 Jimison, L. H. *et al.* Measurement of Barrier Tissue Integrity with an Organic Electrochemical Transistor. *Adv. Mater.* **24**, 5919-5923 (2012).

4 Lieberth, K. *et al.* Monitoring Reversible Tight Junction Modulation with a Current-Driven Organic Electrochemical Transistor. *Adv. Mater. Technol.* **6**, 5, 2000940 (2021).

5 Mulaosmanovic, H., Chicca, E., Bertele, M., Mikolajick, T. & Slesazeck, S. Mimicking biological neurons with a nanoscale ferroelectric transistor. *Nanoscale* **10**, 21755-21763 (2018).

6 Inagaki, T. *et al.* Collective and synchronous dynamics of photonic spiking neurons. *Nat. Commun.* **12**, 2325 (2021).

7 Torrejon, J. *et al.* Neuromorphic computing with nanoscale spintronic oscillators. *Nature* **547**, 428-431 (2017).

8 Abu-Hassan, K. *et al.* Optimal solid state neurons. *Nat. Commun.* **10**, 5309 (2019).

9 Hao, S. *et al.* A Monolayer Leaky Integrate-and-Fire Neuron for 2D Memristive Neuromorphic Networks. *Adv. Electron. Mater.* **6**, 4, 1901335 (2020).

10 Bohaichuk, S. M. *et al.* Fast Spiking of a Mott VO2–Carbon Nanotube Composite Device. *Nano Lett.* **19**, 10, 6751-6755 (2019).

11 Yi, W. *et al.* Biological plausibility and stochasticity in scalable VO(2) active memristor neurons. *Nat. Commun.* **9**, 4661-4661 (2018).

12 Zhang, X. *et al.* An artificial spiking afferent nerve based on Mott memristors for neurorobotics. *Nat. Commun.* **11**, 51 (2020).

13 Park, S.-O., Jeong, H., Park, J., Bae, J. & Choi, S. Experimental demonstration of highly reliable dynamic memristor for artificial neuron and neuromorphic computing. *Nat. Commun.* **13**, 2888 (2022).

14 Pickett, M. D., Medeiros-Ribeiro, G. & Williams, R. S. A scalable neuristor built with Mott memristors. *Nat. Mater.* **12**, 114-117 (2013).

15 Kumar, S., Strachan, J. P. & Williams, R. S. Chaotic dynamics in nanoscale NbO2 Mott memristors for analogue computing. *Nature* **548**, 318-321 (2017).

16 Kumar, S., Williams, R. S. & Wang, Z. Third-order nanocircuit elements for neuromorphic engineering. *Nature* **585** (2020).

17 Tee, B. C.-K. *et al.* A skin-inspired organic digital mechanoreceptor. *Science* **350**, 313-316 (2015).

18 Mirshojaeian Hosseini, M. J. *et al.* Organic electronics Axon-Hillock neuromorphic circuit: towards biologically compatible, and physically flexible, integrate-and-fire spiking neural networks. *J. Phys. D: Appl. Phys.* **54**, 104004 (2020).

19 Harikesh, P. C. *et al.* Organic electrochemical neurons and synapses with ion mediated spiking. *Nat. Commun.* **13**, 901 (2022).